PAPER

Check for updates

A soft approach towards composite porous carbon/conducting polymer supercapacitors: layer-by-layer integration of pyrolyzed ZIF-8 MOF and PANI-PSS supramolecular complexes

Ana Paula Mártire, Omar Azzaroni, [iD] Waldemar Marmisolle [iD] * and Matias Rafti [iD] *

Amid the global energy crisis, the search for safe, sustainable, and high-performance energy storage is urgent. Supercapacitors—renowned for their exceptional power density and cycling stability—offer a compelling path forward, especially when engineered with eco-friendly materials and neutral-pH aqueous electrolytes. In this work, we present a simple yet powerful layer-by-layer (LbL) strategy to fabricate supercapacitor electrodes by integrating porous carbon from pyrolyzed ZIF-8 (PCZIF-8) with a polyaniline–polystyrene sulfonate (PANI-PSS) complex. The resulting films were probed *via* cyclic voltammetry and electrochemical quartz crystal microbalance (eQCM) to unravel their charge-storage dynamics, while galvanostatic cycling tested their long-term resilience. The composite film exhibits specific capacitances of 225 F g^{-1} in 0.1 M HCl and 160 F g^{-1} in 0.1 M KCl for 1 A g^{-1} charge–discharge galvanostatic curves. The specific capacitance increased by more than 1000% when a porous carbon was used instead of a non-porous one. The inclusion of PCZIF-8 delivered a substantial performance leap under mild, environmentally benign conditions—all using low-cost, readily synthesized components. This synergy between conductive polymers and porous carbons from MOFs opens a sustainable and scalable route to next-generation energy storage.

Introduction

Supercapacitors (SC) are energy storage devices known for their high power density, rapid charge/discharge rates, and extended cyclability life span.[1] The capacitance can arise from two main sources, namely, the electric double-layer and a pseudocapacitive contribution from redox processes.[2] While electrical double-layer capacitance (EDLC) is a consequence of charge accumulation due to migration of electrolytes under applied voltage, pseudocapacitance stems from fast reversible faradaic reactions taking place at the electrode interface. In this context, numerous combinations of carbon materials with other active components have been explored for electrode modification in supercapacitors.[3–5] The inclusion of porous materials in SC through *ad-hoc* designed nanoarchitectures is an appealing option for performance enhancement (*e.g.*, including porous carbon building blocks).[6–9]

Instituto de Investigaciones Fisicoquímicas Teóricas y Aplicadas (INIFTA),
Departamento de Química, Facultad de Ciencias Exactas, Universidad Nacional de
La Plata-CONICET, La Plata B1904DPI, Argentina.
E-mail: wmarmi@infita.unlp.edu.ar, mrafti@quimica.unlp.edu.ar

Due to the important sustainability requirement, great efforts are currently being devoted to designing SC with low environmental impact, both regarding synthetic procedures and operating conditions.[10] Main challenges for such a goal are the substitution of commonly used hazardous electrolytes and highly corrosive chemicals involved in the synthesis and activation of porous materials.[11] A way to tackle the above-discussed issues would be, for example, to obtain porous carbon materials using synthetic procedures that do not require harsh activation, and ideally, integrating them into electrochemical systems that could operate efficiently with aqueous neutral electrolytes.[12]

Thinking of possible ways to address the above challenges, metal organic frameworks (MOFs) become an interesting option. MOFs are crystalline solids composed of metal ions coordinated with organic linkers into high surface area, non-covalent porous networks that yield porous carbon particles when pyrolyzed under appropriate conditions.[9,13–15] MOFs are extensively used in energy-related applications due to their tuneable pore-wall chemistry, high surface areas, and the possibility of controlling particle size and morphology.[16] Most common applications use pyrolyzed MOFs for SC assembly due to

their dielectric nature; however, the number of conductive MOFs reported is rapidly increasing, thus opening new paths for innovation in this regard.[17,18] Pyrolysis conditions and parent MOF chosen are decisive for the resulting material and must be tuned accordingly. For example, relatively low temperatures (up to 600 °C) render incomplete carbonization and partial elimination of common carbon templates added. Although high temperature pyrolysis (up to 1000 °C) favours the appearance of additional porosity due to increased graphitization and elimination of metal atoms present, excessive and fast heating can cause the collapse of the porous network together with loss of heteroatoms from MOF linkers, which in turn reduces nanocarbon conductivity.[19–21]

One of the most visited MOF subclasses for this and other related applications is the so-called zeolite imidazolate frameworks (ZIFs), built from the combination of N-bidentate imidazole linkers and tetrahedrally coordinated M^{2+} metal ions (e.g., M = Co, Zn).[22] Depending on the actual imidazole ring present, ZIF materials receive a distinctive number added to the acronym for their identification. A particularly popular member is the material composed of 2-methyl-imidazolate linkers, known as ZIF-8, which due to its biocompatibility, relatively high thermal/chemical stability, and both varied and straightforward synthesis with inexpensive chemicals and solvents, has been employed for several different applications ranging from catalysis to separations and optics[23–27] Since pioneering reports from almost a decade ago, there have been multiple efforts oriented to establishing protocols for controlled production of micro/mesoporous carbon from ZIF-8 (PCZIF-8) that could be employed in the assembly of electroactive nanoarchitectures.[23,28–33]

One of the main issues to be addressed in the assembly of PCZIF-8 SC electrodes is ensuring mechanical stability and electrochemical connectivity when processed into films. Conducting polymers (CPs) such as poly(3,4-ethylenedioxythiophene) (PEDOT) or polyaniline (PANI) and their complexes with other polymers like poly(styrenesulfonate) (PSS) offer a compelling solution, as they can provide both adhesion and additional electrochemical activity[34–36] The combination can be achieved through several approaches, e.g., by carrying surface chemical polymerization of aniline in the presence of colloidal PCZIF-8 (yielding core@shell nanoarchitectures),[37] via mixing with (PEDOT:PSS),[36,38] or by creating porous carbon covered PANI fibres, which are then deposited on a conductive electrode substrate.[39,40] Another reported method incorporates both PANI and ZIF-8 into an aerogel matrix, which is subsequently co-carbonized within the aerogel structure.[41]

In all the above-discussed approaches, the porous carbon nanomaterial needs to be processed using adequate solvents, deposited, and then dried before the SC can be subjected to electrochemical testing. Our contribution aims to demonstrate a sequential soft assembly of SC components, which can also

perform under neutral aqueous electrolyte. For this end, we took advantage of our previous experience with electrode–electrolyte interface engineering via layer-by-layer (LbL) assembly, enabling thus precise control over film architecture by alternately depositing positively and negatively charged species, thereby promoting intimate contact in well-organized hybrid three-dimensional structures.[42–45] Aqueous near-neutral conditions employed are appealing to the environmental impact of the approach; however, poses a challenge due to PANI's limited electroactivity.[46,47] To overcome this limitation, we included instead (PANI:PSS) complexes obtained through ad-hoc template polymerization, improving stability and procesability.[48–50] Following previously explored approaches, we propose the use of ZIF-8 MOF-derived porous carbon using commercial non-porous graphitic carbon as a benchmark.[51,52]

Films obtained via LbL were investigated by a combination of cyclic voltammetry and galvanostatic charge–discharge experiments. Their electrochemical capacitance and process dynamics were studied using a quartz crystal microbalance (QCM and eQCM). This work shows that the incorporation of porous carbon nanoparticles into (PANI:PSS) composite films increase the EDLC contribution to the electrode's capacitance and significantly improves its electrochemical response. This approach presents a promising pathway to develop high-performance, neutral-electrolyte supercapacitors with improved efficiency and durability.

Experimental section

Chemicals

Aniline, ammonium persulfate (APS), poly (sodium 4-styrene sulfonate) (PSS) (Mw ≈ 70 kDa), polyallylamine hydrochloride (PAH) (ca. 17.5 kDa), polyethylenimine (PEI) (50% in H_2O, Mw ≈ 750 kDa), $Zn(NO_3)_2 \cdot 6H_2O$, 2-methyl-imidazole (2 m-Im), and (1-hexadecyl)trimethyl-ammonium bromide (99%) (CTAB) were purchased from Sigma-Aldrich. Expanded graphite was purchased from Carbone Lorraine. Methanol was obtained from Dorwil. Hydrochloric acid and potassium chloride were purchased from Anedra. All chemicals were employed as received except for aniline which was distilled and methanol which was dried and distilled as reported before.[53] All solutions were prepared with deionized water (18.2 MΩ cm).

ZIF-8 synthesis

ZIF-8 was obtained as reported before by mixing 250 ml of 25 mM $Zn(NO_3)_2$ and 250 ml of 100 mM 2 m-Im solutions prepared with anhydrous methanol.[54] The reaction batch was stirred at 25 °C for four hours and the colorless liquid turned white. Then, most of the solvent was extracted using the rotary evaporator at 40 °C and 250 mbar for three hours. Next, the sample was collected via centrifugation (11 400

rpm, 10 minutes), washed twice with fresh methanol, and dried overnight at 60 °C.

PCZIF-8 synthesis

ZIF-8 was pyrolyzed under flowing N_2. First, the sample was dried for 2 h at 100 °C and 2 h at 200 °C. Second, the burning occurred during 4 h at 750 °C. All these temperatures were achieved with a heating rate of 10 °C min^{-1}. Finally, a black powder was obtained indicating the presence of the ZIF-8 derived porous carbon (PCZIF-8).

PCZIF-8 dispersions

The PCZIF-8 was dispersed in DI water by probe sonication in the presence of CTAB. The PCZIF-8 concentration was 1 mg mL^{-1}. Two concentrations of CTAB were used: 10 mg ml^{-1} (C1) and 20 mg ml^{-1} (C2). The solution was ultrasonicated for 30 minutes in a beaker before being used in the LbL assembly process.

GC dispersion

A graphitic carbon (GC) previously characterized was used in this work.[51] Its dispersion was prepared with 10 mg ml^{-1} of CTAB and 1 mg mL^{-1} of carbon. The dispersion was ultrasonicated (probe sonication) for 30 minutes in a beaker before being used in the LbL assembly process.

PANI-PSS synthesis

The PANI-PSS dispersion was prepared by chemically polymerizing aniline in the presence of PSS. Firstly, a 5 mM aniline solution in 0.5 M HCl was prepared. Then, PSS was added to reach a 5 mM concentration. After 15 minutes of stirring, APS was added to reach a 5 mM concentration, and the solution was stirred overnight. The synthesis was carried out in 40 mL falcon tubes, with a final volume of 20 mL. The preparation color was initially dark blue and then turned green.

PANI-PSS dispersions

On the one hand, the batch synthesis was diluted 1/10 in 0.5 M HCl (A PANI-PSS) and used in the LbL assembly. On the other hand, the batch synthesis was neutralized with 10% KOH up to pH 7 and diluted 1/10 with DI water (N PANI-PSS) for use in the LbL assembly.

Layer-by-layer assembly

The LbL assembly integrated PCZIF-8 in C1 or C2 dispersion with acid or neutral PANI-PSS dispersion in the four possible combinations. A general process starts with a previously cleaned Au or glass substrate followed by a 10-minute immersion in 1 mg mL^{-1} PEI solution and a 5-minute rinse in DI water. Next, the substrates were dipped in the PANI-PSS dispersion for 10 minutes, and 5 min-washed with HCl 0.5 M for A PANI-PSS or DI water for N PANI-PSS. Then, the substrates were immersed in the PCZIF-8 dispersion and rinsed for 5 minutes in DI water. This sequence yielded a single bilayer, and the n times repetitions were carried out to obtain a [PANI-PSS/PCZIF-8]n assembly, where n means the number of bilayers.

Characterization/electrochemical measurements

Nitrogen adsorption. N_2 adsorption isotherms were carried out with a ASAP 2020 HD88 surface area and porosity analyser from Micromeritics.

XPS. X-ray photoelectron spectroscopy (XPS) was performed using a Proven X-PS from SPECS. The Mg Kα (1253.6 eV) X-ray source was employed.

UV-vis spectroscopy. UV-vis measurements were performed by assembling the LbL on a glass slide. Spectra were taken using an Agilent model 8453E diode array spectrophotometer.

DLS and zeta potential. ZetaSizer Nano, Nano ZSizer-ZEN3600, from Malvern was employed for dynamic light scattering (DLS) and zeta potential (Zpot). To determine the Zpot, electrophoretic mobility was measured by laser Doppler velocimetry. Disposable capillary cells (DTS 1061 1070, Malvern) were used at 25 °C. A drive cell voltage of 30 V was applied and the monomodal analysis method was used.

Electrochemical measurements. A Gamry Reference 600 potentiostat was used to measure the cyclic voltammetry and charge–discharge curves. A three-electrode setup was employed, using a Pt wire as a counter electrode and an Ag/AgCl (3 M NaCl) electrode as a reference. Au substrates, prepared by Au sputtering on glass, were used as working electrodes.

Raman. Raman spectroscopy measurements were performed with a BWTek Raman spectrometer (BWS415-532S) equipped with an optical microscope (BAC151B model). PANI-PSS dispersion was measured as a liquid, PCZIF-8 as a powder, and the assemblies on top of an Au surface. The applied excitation wavelength was 785 nm with a laser power ranging from 50 to 250 mW.

SEM. SEM images of the PCZIF and the assemblies were taken with an ESEM FEI Quanta 200 microscope. For SEM sample preparation, the PCZIF-8 dispersion was diluted 1/10 with DI water. The diluted dispersion and the assembly were on top of an Au surface. Samples did not require metallization.

QCM dry mass measurements. Quartz crystal microbalance (QCM) measurements were conducted using a QCM 200 (Stanford Research Systems) with commercially available gold-coated quartz sensors (QCM25 5 MHz, sensitivity factor: 56.6 Hz cm^2 μg^{-1}). The LbL assembly was applied to the sensors to monitor dry mass growth.

Electrochemical QCM (eQCM). The combined electrochemical and mass measurements were performed with an eQCM 10 M™ Impedance Scanning Electrochemical Quartz Crystal Microbalance from Gamry Instruments, complementing the Gamry Reference 600 potentiostat. Gold-coated commercial quartz sensors were purchased from Gamry Instruments (#971-00006, 10 MHz, sensitivity factor: 226 Hz

cm^2 μg^{-1}). The LbL assembly procedure was performed *in situ* on the sensors. A three-electrode arrangement was employed in a Teflon cell, using a Pt wire and an Ag/AgCl (3 M NaCl) as counter and reference electrodes.

Results and discussion

ZIF-8 pyrolysis

Firstly, ZIF-8 was synthesised to produce porous carbon. The ZIF-8 was prepared as reported before by mixing methanolic solutions of $Zn(NO_3)_2$ and 2-methylimidazole. The resulting white product was characterised using wide-angle X-ray scattering (WAXS), and the results confirm the match between calculated and experimental peaks, verifying the presence of the ZIF-8 phase (Fig. S1). Thermogravimetric analysis (TGA) was also conducted to assess thermal stability under a nitrogen atmosphere. The thermal decomposition of ZIF-8 occurred at 450 °C, consistent with previous reports (Fig. S2).[22]

Next, the sample underwent pyrolysis at 750 C for 4 hours in a nitrogen atmosphere, resulting in a black powder identified as ZIF-8 porous carbon (PCZIF-8). This process is illustrated in Fig. 1A. The N_2 adsorption isotherms for both ZIF-8 and PCZIF-8 were measured (Fig. 1B), and BET surface area analysis (Fig. S3) revealed values of 1475 m^2 g^{-1} for fresh ZIF-8 and 875 m^2 g^{-1} for the pyrolyzed material. The adsorption isotherm of the PCZIF-8 also revealed, in addition to the preserved microporosity, a characteristic hysteresis loop indicative of mesoporosity. Although some reduction in surface area is to be expected from pyrolysis, the value obtained is relatively lower compared to other reported protocols. This can be understood considering that, although the selected temperature is high enough to cause graphitization and conversion into amorphous carbon (see Raman spectra below), yet low enough to ensure the preservation of both N and Zn heteroatoms in the PCZIF-8. We have selected this temperature, which represents an optimal balance between the upper and lower pyrolysis limits, in order to preserve the conductivity and microporosity of the material obtained, features that contribute to the enhancement of SC performances.

To analyse the composition of PCZIF-8, X-ray photoelectron spectroscopy (XPS) was used, focusing on the Zn (Fig. 1C) and N (1D) binding energy regions. Two oxidation states of Zn were identified: Zn^{2+} at 1046.22 and 1023 eV, and Zn^0 at 044.75 and 1021.7 eV. Additionally, pyridinic, pyrrolic, and graphitic nitrogen were detected at 398.3, 399.67, and 400.9 eV, respectively. These results confirm that PCZIF-8 is a porous carbon material with a high surface area including nitrogen and zinc into its porous matrix.
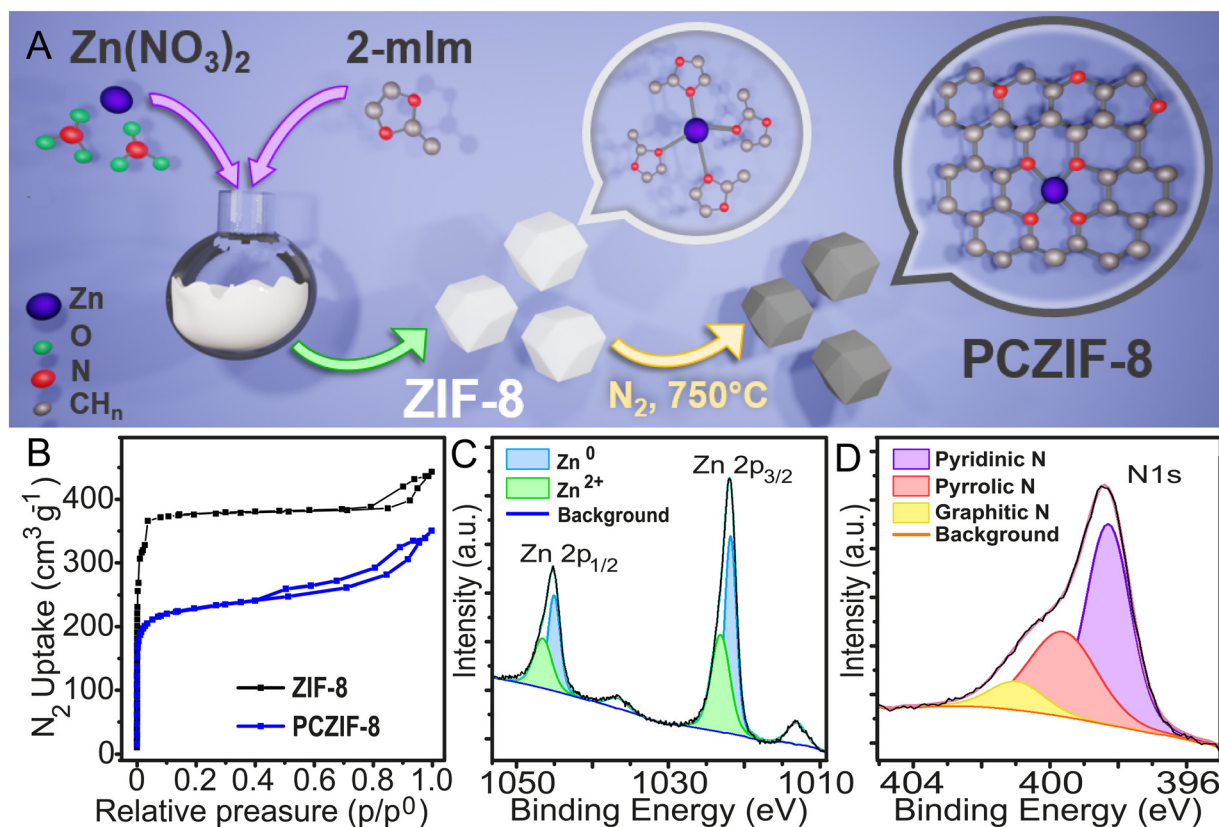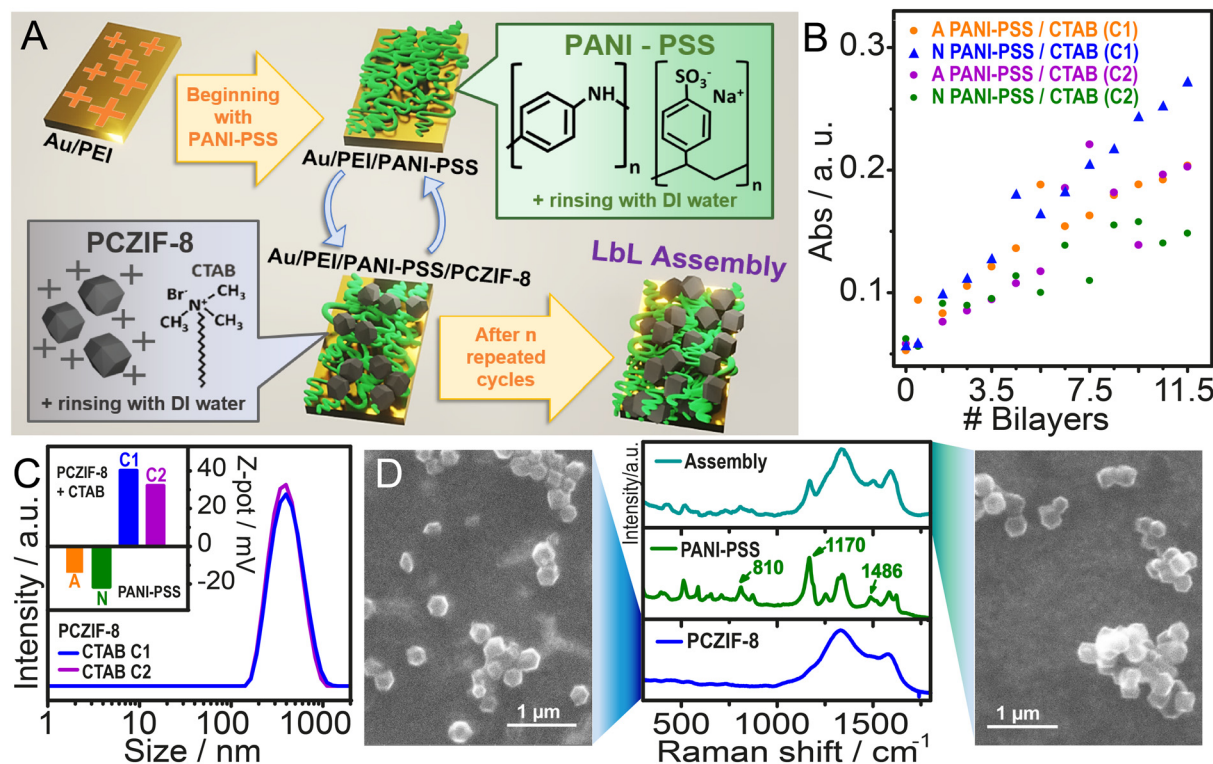

Fig. 1 (A) Scheme of the synthesis of PCZIF-8. (B) N_2 adsorption isotherm for ZIF-8 and PCZIF-8. (C) XPS Zn 2p band and (D) N 1s band for PCZIF-8.

Fig. 2 (A) Assembly process combining PCZIF-8 with PANI-PSS. (B) Absorbance at 750 nm for an increasing number of deposition cycles comparing four different assembly conditions varying PANI-PSS pH and the CTAB concentration used to disperse the PCZIF-8. (C) Intensity averaged DLS for the PCZIF-8 dispersions used in the assemblies. (Inset C) Z-potential of the colloidal suspensions used for the LbL. (D) Raman spectra of PANI-PSS, PCZIF-8, and the assembly. Pictures in black and white correspond to SEM images from PCZIF-8 dispersion and the LbL assembly.

Layer-by-layer assembly

The Layer-by-Layer (LbL) technique was selected to construct hybrid films that integrate PCZIF-8 dispersions with conductive polymer complexes (PANI-PSS), as depicted in Fig. 2A. PCZIF-8 was previously dispersed in CTAB solutions by probe sonication. The LbL process begins with a clean gold substrate, onto which a layer of PEI is first deposited. Following this, alternate soaking in PANI-PSS and PCZIF-8/CTAB dispersions was performed to build the LbL assembly.

To optimise the conditions for film growth, different assembly conditions were tested. PCZIF-8 was dispersed in water using two concentrations of CTAB: 10 mg ml^{-1} (C1) and 20 mg ml^{-1} (C2). The PANI-PSS dispersion was prepared in two forms: acidic (diluted in 0.5 M HCl) and neutral (neutralised with KOH and then diluted in deionized water). These variables were combined to create four different systems, which were tested by growing films on clean glass substrates and measuring absorbance at 750 nm, at which PANI-PSS shows maximum absorption (Fig. 2B). Absorbance increased with each deposition cycle for all four systems. However, the most consistent and regular growth was observed in the system combining neutral PANI-PSS with PCZIF-8 dispersed in C1. This system was selected for further experiments.

The prepared dispersions were analysed using Z-potential measurements (Fig. 2C). The PCZIF-8 dispersions had a

Z-potential of +40.2 mV (C1) and, +32.2 mV (C2). In contrast, the neutral PANI-PSS dispersion showed a Z-potential of −21.6 mV and, acidic PANI-PSS -13.8 mV. These opposite surface charges confirm that electrostatic interactions make the LbL assembly feasible. Additionally, the size of the dispersed meso-microporous carbon particles was measured using dynamic light scattering (DLS), revealing a hydrodynamic size of 440 nm in diameter for both CTAB concentrations.

Next, the film produced and each component were studied by Raman spectroscopy (Fig. 2D). For the PCZIF-8 a typical graphitic carbon spectrum was observed: the G band associated with the ordered sp^2 structure at 1570 cm^{-1} and the D band related to the defective structure at 1330 cm^{-1}.[55–57] The ratio $I_G/I_D = 0.3$ is indicative of a graphitic-type material. In the PANI-PSS sample three characteristic signals were identified: at 810 and 1170 cm^{-1} the C–H bending in the quinoid and benzenic ring and at 1486 cm^{-1} the C=N stretching.[51] These five signals could also be observed in the assembly spectrum, confirming the presence of PANI-PSS and PCZIF-8 in the composite film.

To further characterise the PCZIF-8 dispersion and the assembly, microscopic images were taken with a scanning electron microscope (SEM). Fig. 2D (left), shows the PCZIF-8 dispersion deposited on a clean Au surface. The PCZIF-8 were identified as monodispersed polyhedrons with an average

particle size of 290 ± 30 nm (*n* = 138). The same particles were observed in clusters in the LbL assembly (Fig. 2D, right) confirming the PCZIF-8 integration in the film.

Electrochemical comparison between PCZIF-8 and graphitic carbon.

The electroactivity and electrochemical connectivity of the LbL films were evaluated through cyclic voltammetry at various stages of the construction process. For this, the assembly was built directly on the Au electrode in the Teflon electrochemical cell, and cyclic voltammograms were recorded after each PANI-PSS step deposition. Fig. 3A and S4 present cyclic voltammograms corresponding to increasing numbers of bilayers measured in HCl and KCl respectively. A steady increase in current is observed after each deposition cycle, consistent with the trend in Fig. 3B. This behaviour suggests the build-up of an electrochemically interconnected material.

The electrochemical performance of the 11.5 BL assembly with PCZIF-8 was studied at different scan rates (Fig. 3C and D). The peak current showed a linear dependence on the potential scan rate, indicating a surface-confined electrochemical process with no diffusion constraints (inset Fig. 3C and D).[58] For these voltammograms, eqn (1) was applied to calculate the specific voltammetric capacitance:

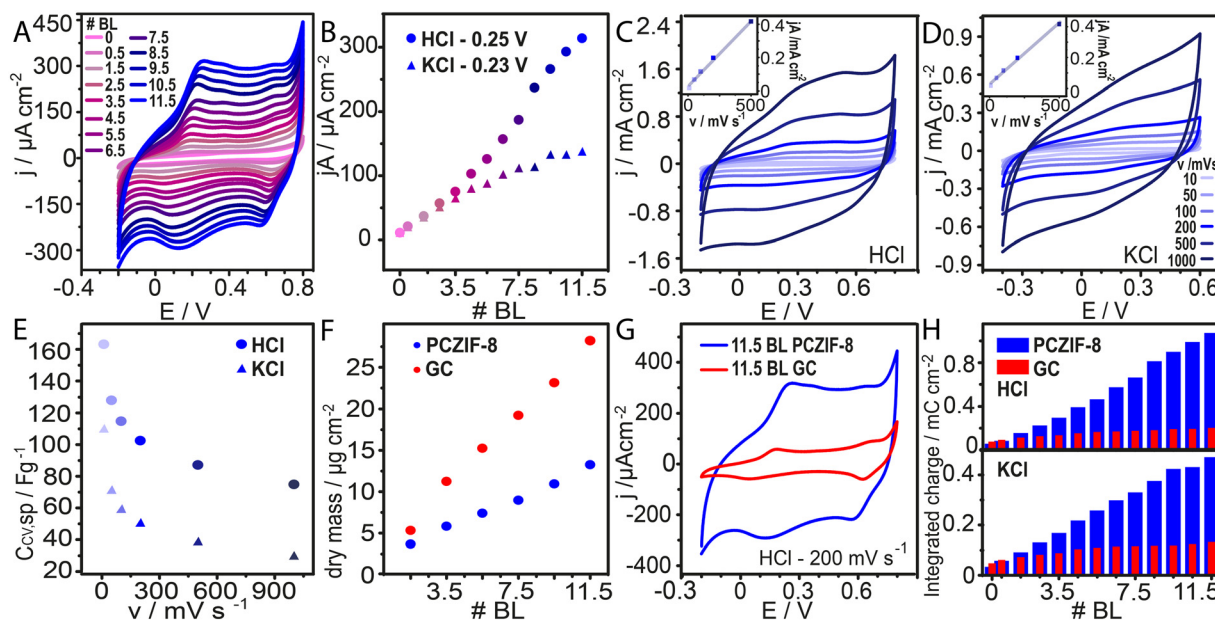$$C_{CV,SP} = \frac{1}{mv(V_f - V_i)} \int_{V_i}^{V_f} I(V)dV \quad (1)$$

In this equation *m* (g) is the dry mass obtained in the QCM experiment, *v* (V s^{-1}) is the scanning rate, $(V_f - V_i)$ (V) is the potential window applied in cyclic voltammetry and *I* (A) is the current measured. The calculated capacitance values, shown in Fig. 3E, reached 163 and 110 F g^{-1} in HCl and KCl, respectively, at a scan rate of 10 mV s^{-1}.

To evaluate the carbon porosity contribution to the film's capacitance, the PCZIF-8 assembly was compared to another assembly prepared with a commercial graphitic carbon (GC) dispersion. The dry mass growth of both films was monitored *via* QCM (Fig. 3F) performing the LbL process on top of a gold QCM sensor. The two systems grew linearly; however, the GC assembly reached higher mass deposition than the PCZIF-8 one.

The electrochemical growth of the GC assembly was also followed by cyclic voltammetry. Fig. S5 displays the voltammograms for this film with increasing deposition cycles. The comparison of the voltammograms of 11.5 bilayers for the two systems is presented in Fig. 3G and S6 for 0.1 M HCl and 0.1 M KCl, respectively. The performance observed was notably different; although the PCZIF-8 assembly has less deposited material, it exhibits a much higher voltammetric current response than the GC films.

Integrated charge calculations (Fig. 3H) further highlight these differences: charge increased substantially with bilayer number in PCZIF-8 films but remained nearly constant for GC assemblies.

Specific capacitance values at different scan rates for both 11.5 BL assemblies are summarized in Table S1. These results indicate that the carbon porosity enhances the

Fig. 3 (A) Cyclic voltammograms of the assembly PANI-PSS/PCZIF-8 after different number of deposition cycles scanning in 0.1 M HCl at 200 mV s^{-1}. (B) Anodic peak current density values for the PCZIF-8 growing films at 200 mV s^{-1}. Cyclic voltammograms at different scan rates for an 11.5-bilayer assembly PANI-PSS/PCZIF-8 in (C) 0.1 M HCl and (D) 0.1 M KCl. (Inset C and D) anodic peak current density values at different scan rates. (E) Corresponding specific voltammetric capacitance values. (F) QCM dry mass measurements at different stages of the LbL assembly process for PCZIF-8 and GC. (G) Cyclic voltammograms from an 11.5-bilayer assembly using PCZIF-8 or GC in 0.1 M HCl. (H) Integrated charge with increasing bilayers in the assembly process for PCZIF-8 and GC at 200 mV s^{-1}.

electrochemical capacity, leading to an efficient performance even in lighter films.

Specific voltammetric capacitance values were also compared across different number of bilayers in Fig. S7. The disparity in electrochemical performance between the two systems becomes more pronounced when comparing specific capacitance, as GC film has a higher mass and a lower current response than the PCZIF-8 one. Furthermore, for PCZIF-8 assembly, a nearly constant specific capacitance values with increasing bilayers are observed. This trend indicates electrochemically interconnected material inclusion.

Analysis of the capacitance components

Next, to evaluate the effects contributing to the assembly's capacitance, the Trasatti and Dunn methods were employed.[59,60] First, the Trasatti method considers the total capacitance (C_T) as an addition of two contributions shown in eqn (2):

$$C_T = C_c + C_d \tag{2}$$

In this equation C_c is the electric double layer capacitance and C_d is the pseudocapacitance.[4,61] The capacitance increases with decreasing scan rate; thus, the capacitance attributed to the total surface area can be estimated from eqn (3) by extrapolating to zero scan rate:

$$\frac{1}{C_{CV,SP}} = \frac{1}{C_T} + k_1 v^{1/2} \tag{3}$$

In this equation, v is the scan rate, k_1 is a constant and $C_{CV,SP}$ is the specific capacitance calculated at each scan rate.

Assuming that C_c is independent of the scan rate, its value can be determined from eqn (4) by extrapolating to the infinite-scan rate limit.

$$C_{CV,SP} = C_c + k_2 v^{-1/2} \tag{4}$$

In this equation, k_2 is another constant. Fig. 4A and B show the plots from eqn (3) and (4), respectively. $C_{CV,SP}$ was analysed for scan rates from 10 to 500 mV s^{-1}.

Second, Dunn method was applied, analysing the behaviour of the current density (j) with the scan rate. The dependence of j on v is expressed in eqn (5):
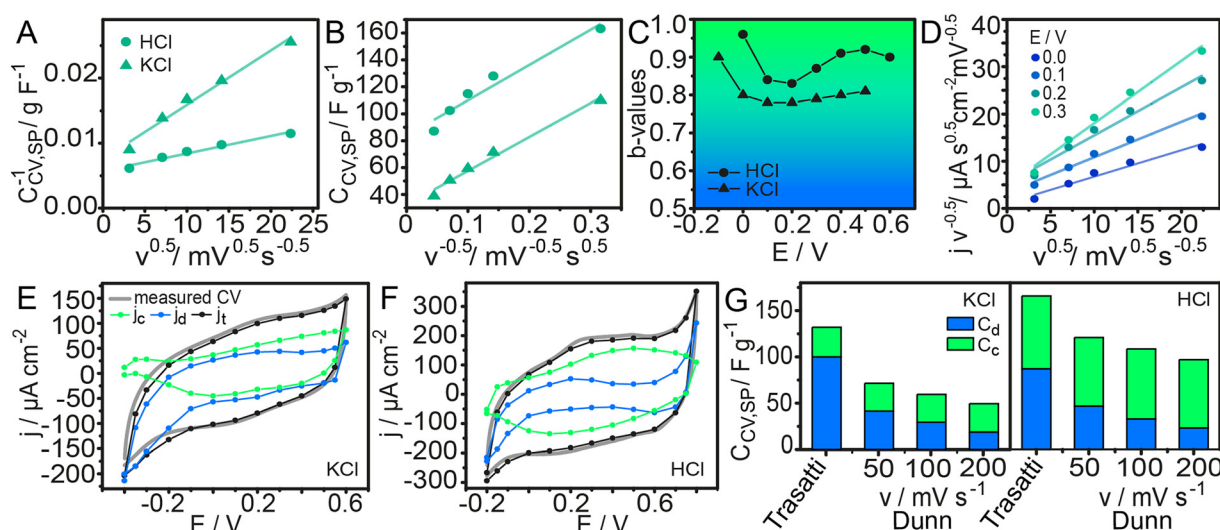
$$j = av^b \tag{5}$$

In eqn (5), a and b are constants. Two characteristic b values are commonly recognized: $b = 0.5$ for diffusion-controlled processes and $b = 1$ for capacitive behaviour. The b value for our assemblies was determined, applying log to eqn (5):

$$\log(j) = \log(a) + b \log(v) \tag{6}$$

The linear regression fitting for $\log(j)$ vs. $\log(v)$ is shown in Fig. S8. The b values obtained for our assemblies in KCl and HCl solutions are shown in Fig. 4C. All b values range between 0.78 and 0.97. Although this indicates a combination of contributions to the current density and b is not strictly equal to 1, according to previous reports, the overall behaviour of the composite film can be considered characteristic of a supercapacitor.[62,63]

Thus, the total current density can be expressed as the sum of two components, as shown in eqn (7):

$$j_T = j_c + j_d \tag{7}$$

Fig. 4 (A) Dependence of the inverse of the specific capacitance with $v^{0.5}$. (B) Dependence of the specific capacitance with $v^{-0.5}$. (C) b-Values calculated from the slope of eqn (6). (D) $j\ v^{-0.5}$ with $v^{0.5}$ with their linear regression fitting used to obtain k'_1 and k'_2 in 0.1 M HCl. Cyclic voltammograms for 100 mV s^{-1} with j_d and j_c contributions for (E) KCl and (F) HCl. (G) Specific capacitance contributions calculated by the Trasatti and Dunn methods in 0.1 M KCl and 0.1 M HCl.

The total density current (j_T) is composed by the diffusion-controlled current density (j_d, $b = 0.5$) and the capacitive current density (j_c, $b = 1$). Based on these b values, eqn (8) is obtained:

$$j = k_1' v + k_2' v^{1/2} \tag{8}$$

Here, k_1' and k_2' are constants. Dividing the equation by $v^{1/2}$ allows expressing the relationship in linear form, as given in eqn (9).

$$\frac{j}{v^{1/2}} = k_1' v^{1/2} + k_2' \tag{9}$$

Fig. 4D and S9 display representative linear regressions obtained from eqn (9) using HCl and KCl as electrolyte. From the k_1' and k_2' values determined along the voltammetric cycle, the diffusion-controlled (j_d) and capacitive (j_c) current profiles were reconstructed for each voltammogram. Results for 100 mV s^{-1} in KCl and HCl are shown in Fig. 4E and F, while those for 50 and 200 mV s^{-1} are shown in Fig. S10. Integration of each curve allowed the calculation of the specific capacitance corresponding to each contribution (C_d and C_c) at different scan rates. Fig. 4G summarizes these results along with those obtained from the Trasatti method.

As shown in Fig. 4G, the component analysis indicates that, regardless of the scan rates or the specific methods used for evaluation, the differences in capacitance between acidic and neutral media are mainly attributed to the C_c component. This contribution is commonly associated with EDL processes and, in this type of system has a great influence from the PANI block, which constitutes a conducting component.[64,65] Polyaniline exhibits a more pronounced electrical conductivity under acidic conditions; therefore, it is reasonable that composite materials containing PANI display a stronger EDL contribution to the overall capacitance in acidic media. On the other hand, the components that vary linearly with the square root of the scan rate are typically assigned to diffusive processes.[66,67] In the materials developed here, although polyaniline contributes partially to this capacitive behaviour, the main contributors to the linear (capacitive) component are the carbon-based nanomaterials. However, no major differences in this contribution are expected when switching from acidic to neutral media.

Ionic exchange during cyclic voltammetry

During electrochemical switching, the oxidation states of the film components change, leading to the exchange of charged species and solvent captured in the polymer matrix with the electrolyte solution.[68,69] To quantify this exchange, eQCM experiments were performed, combining frequency measurements with cyclic voltammetry. Fig. 5A and S11 show the current and mass change, calculated with the Sauerbrey model, in 0.1 M HCl for 50 and 200 mV s^{-1} scan rates. The observed trend shows a decrease in film mass during oxidation and an increase during reduction.

As already reported, PANI-PSS has a negative charge excess provided by the polystyrene sulfonate (PSS) polyanion. Negative charge excess was confirmed with the z-potential measured of -21.6 mV. Then, the film is expected to exchange cations as charge carriers with the electrolyte during the redox switching.[70–72] To explain the mass
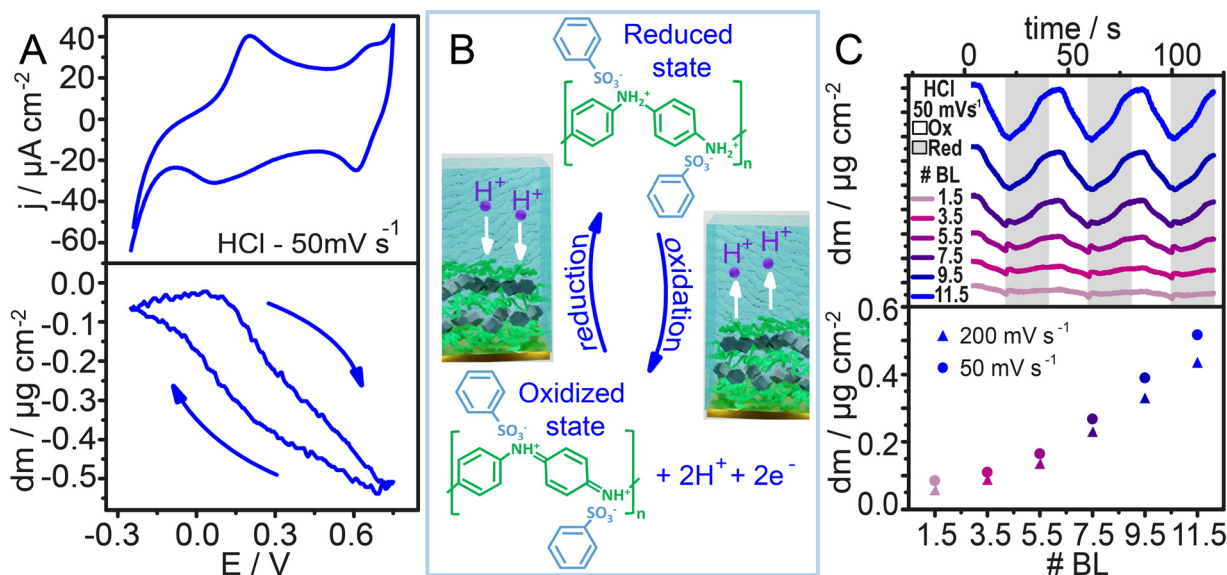

Fig. 5 (A) Cyclic voltammetry and QCM mass change curves for the assembly in 0.1 M HCl at 50 mV s^{-1}. (B) Ionic exchange from the LbL assembly during the redox reaction. (C) Mass change as a function of time during the redox reaction for films of different number of deposition cycles (above). Mass exchange value for the different stages in the assembly process (below).

exchange Fig. 5B illustrates the oxidation and reduction of the film with PANI-PSS considering the cation exchange. Thus, the oxidation releases cations to the solution driving a mass loss and the reduction captures the cations from the solution leading to a mass gain. These exchanged cations are accompanied by solvent molecules, which also modifies the film hydration during redox switching.

The mass exchange was measured after different numbers of deposition cycles of the assembly procedure. Fig. 5C above and S12 represent the mass change with time during cyclic voltammetry performed at 50 and 200 mV s^{-1}. In Fig. 5C mean mass exchange values are shown as a function of the number of deposition cycles. As expected, as the number of deposition steps increases, more conductive polymer is attached to the film and the electrochemical mass exchange increments. This result reinforces the idea that the added material is electrochemically interconnected and exchanging cations and solvent during redox switching.
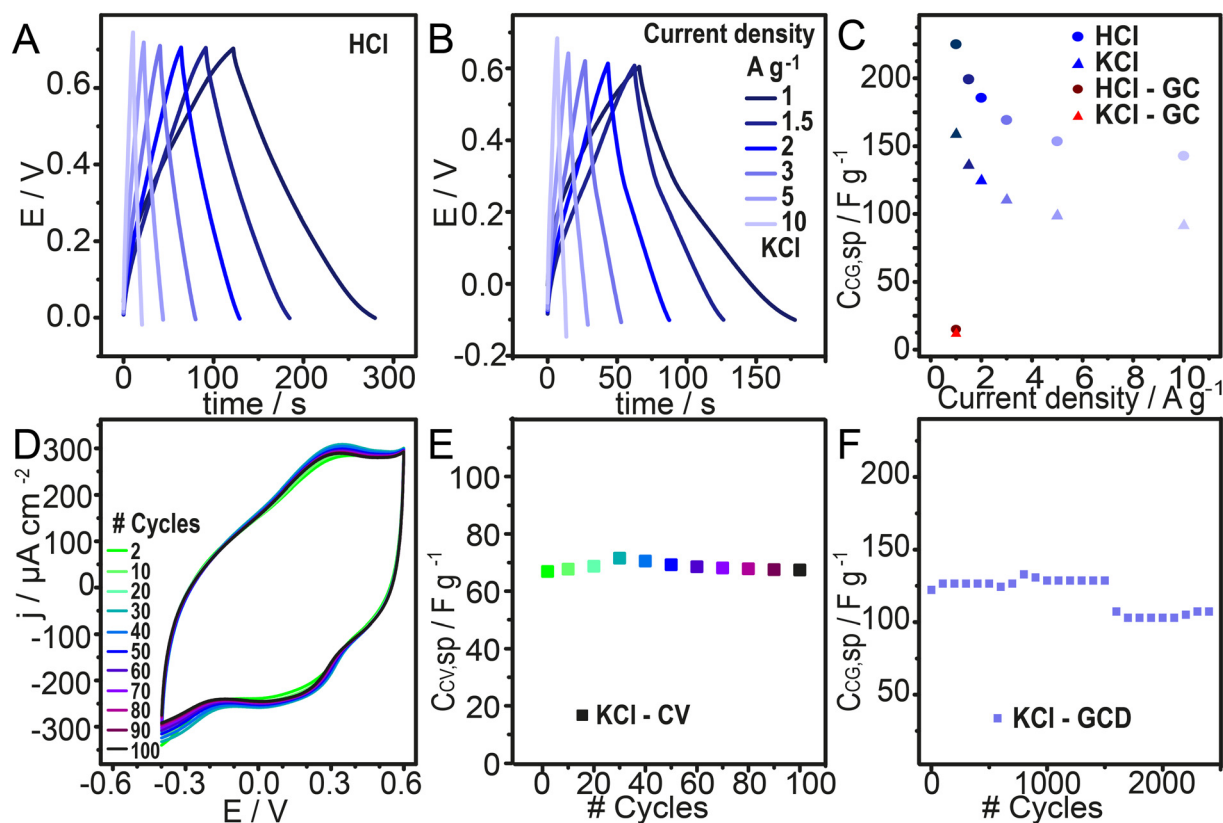
Galvanostatic charge–discharge curves

Galvanostatic charge–discharge cycles were performed at different current densities to study the energy storage in these composite films. The applied current densities were calculated by applying QCM dry mass from Fig. 3F.

Charge–discharge curves are shown in Fig. 6A and B measured in HCl and KCl. Specific capacitance was calculated with eqn (10):

$$C_{CG,SP} = \frac{I\Delta t}{m\Delta V} \qquad (10)$$

where ΔV is the potential window (V), m is the dry mass measured by QCM (g), I is the applied current (A) and Δt is the discharge time (s). $C_{CG,SP}$ values are shown in Fig. 6C. Galvanostatic capacitance values of 225 and 160 Fg^{-1} were obtained at 1 Ag^{-1} in HCl and KCl, respectively. Charge–discharge curves were also carried out for the GC film presenting capacitance values of 15 and 12.85 Fg^{-1} in HCl and KCl, respectively. An increment of more than 1000% is observed in the galvanostatic capacitance values when a porous carbon is included in the electrode–electrolyte interface.

This enhancement is primarily attributed to the increase in the surface area provided by the PCZIF-8 inclusion. The carbon porosity significantly improves ion accessibility, facilitating efficient electrolyte penetration and maximizing the contact between the electrolyte and the conductive material. Another key factor in this improvement is the contribution of the electric double-layer formation, which plays a major role in the charge storage and calculated specific capacitance. In summary, the porous interface not

Fig. 6 Charge and discharge cycles for the 11.5 bilayer PANI-PSS/PCZIF-8 assembly in (A) 0.1 M HCl and (B) 0.1 M KCl. (C) Specific capacitance values for different current densities. (D) Cyclic voltammograms for 100 cycles in 0.1 M KCl at 200 mV s^{-1}. (E) Specific capacitance calculated for 100 curves from cyclic voltammetry. (F) Specific capacitance for charge and discharge cycles up to 2400 cycles.

Table 1 Supercapacitor performance comparison considering works with PCZIF-8

Electrodes using PCZIF-8	Electrolyte	$C_{CG,SP}$ (F g^{-1})	Cycling stability (GCD)	Reference
2 layers PCZIF-8-PANI	1 M H$_2$SO$_4$ – 3 electrodes	322–1 A g^{-1}	100% - 10 000 cycles - 5 mA s^{-1}	37
Core–shell PCZIF-8@PANI	1 M H$_2$SO$_4$ – 2 electrodes	236–1 A g^{-1}	86% - 20 000 cycles - 5 A g^{-1}	39
Aerogel with PANI and ZIF-8 is carbonized	2 M KOH – 3 electrodes	338–0.5 A g^{-1}	91.2% - 5000 cycles - 5 A g^{-1}	41
Co3O4 + PCZIF-8 and PANI polymerized outside	3 M KOH – 3 electrodes	1407–1 A g^{-1}	87.7% - 10 000 cycles - 20 A g^{-1}	40
PCZIF-8 in a Ni foam	2 M KOH – 3 electrodes	187–0.5 A g^{-1}	100% - 10 000 cycles - 5 A g^{-1}	73
ZIF-8 + phytic acid is carbonized	6 M KOH – 3 electrodes	219.4–1 A g^{-1}	100% - 2000 cycles - 5 A g^{-1}	74
ChNF@ZIF-8 is carbonized	6 M KOH – 3 electrodes	182.5–0.2 A g^{-1}	94.8% - 5000 cycles - 1 A g^{-1}	75
CNC@ZIF-8 is carbonized	6 M KOH – 3 electrodes	172–0.1 A g^{-1}	94.5% - 5000 cycles - 0.1 A g^{-1}	76
Layer by layer PCZIF-8/PANI:PSS	0.1 M KCl – 3 electrodes	160–1 A g^{-1}	88% - 2400 cycles - 3 A g^{-1} - 0.1 M KCl	This work
	0.1 M HCl – 3 electrodes	225–1 A g^{-1}		

only enhances ion transport but also reinforces the double-layer capacitance, making the system highly suitable for energy storage applications.

To place our results in context, Tables 1 and S2 compare the specific capacitance values from this work with those reported for PCZIF-8-based and PANI-based supercapacitors. Although the value obtained here is not the highest in the table, it must be highlighted that the other studies operate in more aggressive electrolytes and extreme pH conditions. Considering the environmental friendliness and neutral electrolytes, the capacitance values achieved here are competitive with those of the other systems. Moreover, in several cases, the current densities applied in previous works are lower than those used in these experiments. For comparison at identical current densities, Table S3 presents the results for electrodes cycled at 1 A g^{-1}. These findings emphasized the efficiency of this composed film, which delivers competitive performance without compromising on sustainability.

Film stability and cyclability

The stability in a neutral solution was tested considering the possibility of applying this material to wearable devices. Firstly, 100 cycles of cyclic voltammetry were performed. Fig. 6D shows the voltammograms, and Fig. 6E displays the integrated charge for these curves. The integrated charge did not decay during these cycles; a 100% capacity retention was observed during this test in 0.1 M KCl. Next, a more challenging experiment to study the cyclability during charge–discharge galvanostatic curves was carried out. Fig. 6F displays the specific capacitance calculated with the charge time. Then, 2400 serial cycles at 3 A g^{-1} were performed and the $C_{CG,SP}$ was calculated by applying eqn (10). A 88% capacity retention was observed after 2400 cycles in 0.1 M KCl.

The prepared PANI-PSS/PCZIF-8 assembly exhibits good stability during electrochemical cycling in a neutral electrolyte, which is crucial for its practical application ensuring a long-term performance. Comparing with stability values of other electrodes shown in Table 1, the capacity retention obtained is very promising. Additionally, the ability to operate in a neutral medium is crucial for including it in wearable and portable energy storage devices. Using 0.1 M KCl makes the system more environmentally friendly, as it avoids the use of corrosive or hazardous electrolytes.

Conclusions

In this work, we successfully obtained a micro and mesoporous carbon material through the pyrolysis of ZIF-8 under environmentally friendly conditions, avoiding the use of highly corrosive chemicals or extreme pH solutions. Using this PCZIF-8, we developed hybrid electrodes via a nanoarchitectonics strategy based on the layer-by-layer (LbL) assembly method, enabling the precise integration of PCZIF-8 with a conductive polymer complex (PANI-PSS). This architecture effectively combines the advantages of both components: the high conductivity, structural stability, and electric double-layer capacitance of the carbon, together with the dual EDLC–pseudocapacitive contributions of PANI-PSS.

Electrochemical analysis revealed that incorporating PCZIF-8—with its high surface area and interconnected pore network—greatly enhanced the specific capacitance of the assemblies in neutral aqueous electrolytes. The abundant porosity facilitates ion transport and maximizes the active surface available for charge storage, while the environmentally benign fabrication route avoids corrosive reagents and extreme pH conditions. These combined advantages demonstrate that the rational use of porous carbons derived from MOFs offers a straightforward, scalable, and sustainable strategy to boost the performance of supercapacitors. Such eco-friendly devices hold strong potential for secure, low-impact energy storage applications, from wearable electronics to portable power systems.

Author contributions

APM: methodology, formal analysis, visualization, writing – original draft. OA: conceptualization, resources, funding acquisition. WAM, MR: conceptualization, writing – review & editing, supervision, project administration, funding acquisition.

Conflicts of interest

There are no conflicts to declare.

Data availability

The data supporting this article have been included as part of the supplementary information (SI). Supplementary information: additional material characterization, control experiments and complementary results. See DOI: https://doi.org/10.1039/d5lf00286a.

Acknowledgements

Notes and references

1 B. E. Conway, *Electrochemical supercapacitors: scientific fundamentals and technological applications*, Springer, 1999.

2 H. Chen, T. N. Cong, W. Yang, C. Tan, Y. Li and Y. Ding, *Prog. Nat. Sci.*, 2009, **19**, 291–312.

3 A. Musa, M. M. Islam, M. A. Bin Hasan Susan and M. M. Islam, *ECS J. Solid State Sci. Technol.*, 2023, **12**, 061005.

4 A. Musa, M. A. Hasan, S. S. Aniv and M. M. Islam, *J. Energy Storage*, 2025, **110**, 115221.

5 M. M. Islam, M. Y. A. Mollah, M. A. B. H. Susan and M. M. Islam, *RSC Adv.*, 2020, **10**, 44884–44891.

6 J. Chmiola, G. Yushin, Y. Gogotsi, C. Portet, P. Simon and P. L. Taberna, *Science*, 2006, **313**, 1760–1763.

7 X. Liu, D. Lyu, C. Merlet, M. J. A. Leesmith, X. Hua, Z. Xu, C. P. Grey and A. C. Forse, *Science*, 2024, **384**, 321–325.

8 M. Sevilla and A. B. Fuertes, *Carbon*, 2006, **44**, 468–474.

9 R. R. Salunkhe, Y. V. Kaneti, J. Kim, J. H. Kim and Y. Yamauchi, *Acc. Chem. Res.*, 2016, **49**, 2796–2806.

10 Z. Chang, Y. Yang, M. Li, X. Wang and Y. Wu, *J. Mater. Chem. A*, 2014, **2**, 10739–10755.

11 S. Husien, R. M. El-taweel, A. I. Salim, I. S. Fahim, L. A. Said and A. G. Radwan, *Curr. Res. Green Sustainable Chem.*, 2022, **5**, 100325.

12 G. E. Fenoy, M. Rafti, W. A. Marmisollé and O. Azzaroni, *Mater. Adv.*, 2021, **2**, 7731–7740.

13 X. Chu, F. Meng, T. Deng and W. Zhang, *Nanoscale*, 2021, **13**, 5570–5593.

14 B. Liu, H. Shioyama, T. Akita and Q. Xu, *J. Am. Chem. Soc.*, 2008, **130**, 5390–5391.

15 W. Chaikittisilp, K. Ariga and Y. Yamauchi, *J. Mater. Chem. A*, 2013, **1**, 14–19.

16 M. Arcidiácono, A. P. Mártire, J. A. Allegretto, M. Rafti, W. A. Marmisollé and O. Azzaroni, in *Materials Nanoarchitectonics*, Elsevier, 2024, pp. 387–428.

17 L. S. Xie, G. Skorupskii and M. Dincă, *Chem. Rev.*, 2020, **120**, 8536–8580.

18 L. Niu, T. Wu, M. Chen, L. Yang, J. Yang, Z. Wang, A. A. Kornyshev, H. Jiang, S. Bi and G. Feng, *Adv. Mater.*, 2022, **34**, 2200999.

19 C. Young, R. R. Salunkhe, J. Tang, C.-C. Hu, M. Shahabuddin, E. Yanmaz, M. S. A. Hossain, J. H. Kim and Y. Yamauchi, *Phys. Chem. Chem. Phys.*, 2016, **18**, 29308–29315.

20 Z. Zhao, S. Liu, J. Zhu, J. Xu, L. Li, Z. Huang, C. Zhang and T. Liu, *ACS Appl. Mater. Interfaces*, 2018, **10**, 19871–19880.

21 W. Chaikittisilp, M. Hu, H. Wang, H. S. Huang, T. Fujita, K. C. W. Wu, L. C. Chen, Y. Yamauchi and K. Ariga, *Chem. Commun.*, 2012, **48**, 7259–7261.

22 K. S. Park, Z. Ni, A. P. Cote, J. Y. Choi, R. Huang, F. J. Uribe-Romo, H. K. Chae, M. O'Keeffe and O. M. Yaghi, *Proc. Natl. Acad. Sci. U. S. A.*, 2006, **103**, 10186–10191.

23 J. Tang, R. R. Salunkhe, J. Liu, N. L. Torad, M. Imura, S. Furukawa and Y. Yamauchi, *J. Am. Chem. Soc.*, 2015, **137**, 1572–1580.

24 G. Lu and J. T. Hupp, *J. Am. Chem. Soc.*, 2010, **132**, 7832–7833.

25 L. D. Trino, L. G. S. Albano, D. C. Granato, A. G. Santana, D. H. S. de Camargo, C. C. Correa, C. C. Bof Bufon and A. F. Paes Leme, *Chem. Mater.*, 2021, **33**, 1293–1306.

26 Z. Jiang, H. Liu, S. A. Ahmed, S. Hanif, S. Ren, J. Xu, H. Chen, X. Xia and K. Wang, *Angew. Chem., Int. Ed.*, 2017, **56**, 4767–4771.

27 G. E. Fenoy, J. Scotto, J. Azcárate, M. Rafti, W. A. Marmisollé and O. Azzaroni, *ACS Appl. Energy Mater.*, 2018, **1**, acsaem.8b01021.

28 S. Ma, G. A. Goenaga, A. V. Call and D. Liu, *Chem. – Eur. J.*, 2011, **17**, 2063–2067.

29 Q. Lai, Y. Zhao, Y. Liang, J. He and J. Chen, *Adv. Funct. Mater.*, 2016, **26**, 8334–8344.

30 J. Liu, D. Zhu, C. Guo, A. Vasileff and S. Qiao, *Adv. Energy Mater.*, 2017, **7**, 1700518.

31 H. Zhong, J. Wang, Y. Zhang, W. Xu, W. Xing, D. Xu, Y. Zhang and X. Zhang, *Angew. Chem., Int. Ed.*, 2014, **53**, 14235–14239.

32 Y. Liang, J. Guo, H. Zhang, D. J. L. Brett and S. Gadipelli, *Chem. Eng. J.*, 2024, **489**, 151190.

33 N. Kumar, N. Bansal, Y. Yamauchi and R. R. Salunkhe, *Chem. Mater.*, 2022, **34**, 4946–4954.

34 K. Zhang, L. L. Zhang, X. S. Zhao and J. Wu, *Chem. Mater.*, 2010, **22**, 1392–1401.

35 S. B. Aliev, D. G. Samsonenko, E. A. Maksimovskiy, E. O. Fedorovskaya, S. A. Sapchenko and V. P. Fedin, *New J. Chem.*, 2016, **40**, 5306–5312.

36 Y. Ko, Y. J. Lee, D. Kim, U.-H. Lee and J. You, *ACS Appl. Electron. Mater.*, 2024, **6**, 1045–1054.

37 A. Alameen, T. Jin, C. Xue, X. Ma, X. Du and X. Hao, *J. Solid State Electrochem.*, 2021, **25**, 777–787.

38 X. Li, Y. Liu, M. Gao, X. Zhao and K. Cai, *J. Power Sources*, 2023, **580**, 233455.

39 R. R. Salunkhe, J. Tang, N. Kobayashi, J. Kim, Y. Ide, S. Tominaka, J. H. Kim and Y. Yamauchi, *Chem. Sci.*, 2016, **7**, 5704–5713.

40 K. Chhetri, A. P. Tiwari, B. Dahal, G. P. Ojha, T. Mukhiya, M. Lee, T. Kim, S.-H. Chae, A. Muthurasu and H. Y. Kim, *J. Electroanal. Chem.*, 2020, **856**, 113670.

41 M. Shang, X. Zhang, J. Zhang, J. Sun, X. Zhao, S. Yu, X. Liu, B. Liu and X. Yi, *Carbohydr. Polym.*, 2021, **262**, 117966.

42 W. A. Marmisollé, E. Maza, S. Moya and O. Azzaroni, *Electrochim. Acta*, 2016, **210**, 435–444.

43 K. Ariga, J. P. Hill and Q. Ji, *Phys. Chem. Chem. Phys.*, 2007, **9**, 2319.

44 R. M. Iost and F. N. Crespilho, *Biosens. Bioelectron.*, 2012, **31**, 1–10.

45 G. Decher, B. Lehr, K. Lowack, Y. Lvov and J. Schmitt, *Biosens. Bioelectron.*, 1994, **9**, 677–684.

46 A. Muzaffar, M. B. Ahamed and C. M. Hussain, *Smart Supercapacitors*, Elsevier, 2023, pp. 227–254.

47 W.-S. Huang, B. D. Humphrey and A. G. MacDiarmid, *J. Chem. Soc., Faraday Trans.*, 1986, **82**, 2385.

48 G. Challa and Y. Y. Tan, *Pure Appl. Chem.*, 1981, **53**, 627–641.

49 A. M. Bonastre, M. Sosna and P. N. Bartlett, *Phys. Chem. Chem. Phys.*, 2011, **13**, 5365.

50 A. P. Mártire, G. M. Segovia, O. Azzaroni, M. Rafti and W. Marmisollé, *Mol. Syst. Des. Eng.*, 2019, **4**, 893–900.

51 G. E. Fenoy, B. Van der Schueren, J. Scotto, F. Boulmedais, M. R. Ceolín, S. Bégin-Colin, D. Bégin, W. A. Marmisollé and O. Azzaroni, *Electrochim. Acta*, 2018, **283**, 1178–1187.

52 A. P. Mártire, G. E. Fenoy, O. Azzaroni, M. Rafti and W. A. Marmisollé, *RSC Appl. Interfaces*, 2024, **1**, 511–521.

53 J. A. Allegretto, M. Arcidiácono, P. Y. Steinberg, P. C. Angelomé, O. Azzaroni and M. Rafti, *J. Phys. Chem. C*, 2022, **126**, 6724–6735.

54 J. Cravillon, R. Nayuk, S. Springer, A. Feldhoff, K. Huber and M. Wiebcke, *Chem. Mater.*, 2011, **23**, 2130–2141.

55 A. M. Rao, E. Richter, S. Bandow, B. Chase, P. C. Eklund, K. A. Williams, S. Fang, K. R. Subbaswamy, M. Menon, A. Thess, R. E. Smalley, G. Dresselhaus and M. S. Dresselhaus, *Science*, 1997, **275**, 187–191.

56 L. G. Cançado, A. Jorio, E. H. M. Ferreira, F. Stavale, C. A. Achete, R. B. Capaz, M. V. O. Moutinho, A. Lombardo, T. S. Kulmala and A. C. Ferrari, *Nano Lett.*, 2011, **11**, 3190–3196.

57 A. C. Ferrari and D. M. Basko, *Nat. Nanotechnol.*, 2013, **8**, 235–246.

58 A. J. Bard, L. R. Faulkner and H. S. White, *Electrochemical methods: fundamentals and applications*, Wiley, 3rd edn, 2022.

59 S. Ardizzone, G. Fregonara and S. Trasatti, *Electrochim. Acta*, 1990, **35**, 263–267.

60 J. Wang, J. Polleux, J. Lim and B. Dunn, *J. Phys. Chem. C*, 2007, **111**, 14925–14931.

61 N. M. Deyab, M. M. Taha and N. K. Allam, *Nanoscale Adv.*, 2022, **4**, 1387–1393.

62 A. Cymann-Sachajdak, M. Graczyk-Zajac, G. Trykowski and M. Wilamowska-Zawłocka, *Electrochim. Acta*, 2021, **383**, 138356.

63 S. Harish and P. U. Sathyakam, *J. Electron. Mater.*, 2025, **54**, 10858–10872.

64 J.-W. Jeon, S. R. Kwon and J. L. Lutkenhaus, *J. Mater. Chem. A*, 2015, **3**, 3757–3767.

65 T. Liu, L. Finn, M. Yu, H. Wang, T. Zhai, X. Lu, Y. Tong and Y. Li, *Nano Lett.*, 2014, **14**, 2522–2527.

66 O. Fasakin, K. O. Oyedotun, A. A. Mirghni, N. F. Sylla, B. A. Mahmoud and N. Manyala, *Mater. Today Sustain.*, 2024, **28**, 101028.

67 H. Jia, J. Zhu, L. Wang, S. Sang, W. Liu and F. Chong, *J. Power Sources*, 2025, **625**, 235718.

68 G. Inzelt, in *Electroanalytical Methods: Guide to experiments and applications*, ed. F. Scholtz, Springer Berlin Heidelberg, 2010.

69 M. R. Deakin and D. A. Buttry, *Anal. Chem.*, 1989, **61**, 1147A–1154A.

70 L. P. Bauermann and P. N. Bartlett, *Electrochim. Acta*, 2005, **50**, 1537–1546.

71 X. Du, D. Zhang, X. Ma, W. Qiao, Z. Wang, X. Hao and G. Guan, *Electrochim. Acta*, 2018, **282**, 384–394.

72 B. Zhang, X. Du, X. Hao, F. Gao, D. Zhang, C. Liu and G. Guan, *J. Solid State Electrochem.*, 2018, **22**, 2473–2483.

73 J. Wu, X. Zhang, F. Wei, Y. Sui and J. Qi, *Mater. Lett.*, 2020, **258**, 126761.

74 C. Guo, G. Li, Y. Wu, X. Wang, Y. Niu and J. Wu, *Energies*, 2023, **16**, 7232.

75 Z. Shang, X. An, L. Liu, J. Yang, W. Zhang, H. Dai, H. Cao, Q. Xu, H. Liu and Y. Ni, *Carbohydr. Polym.*, 2021, **251**, 117107.

76 Y. Wang, T. Liu, X. Lin, H. Chen, S. Chen, Z. Jiang, Y. Chen, J. Liu, J. Huang and M. Liu, *ACS Sustainable Chem. Eng.*, 2018, **6**, 13932–13939.